Three-dimensional PIV measurement of flow around an arbitrarily moving body

Young Jin Jeon[1#] and Hyung Jin Sung[1*]

[1]Department of Mechanical Engineering, KAIST,
291 Daehak-ro, Yuseong-gu, Daejeon 305-701, Republic of Korea
[#]youngjin.jeon@kaist.ac.kr, young.jin.jeon@univ-poitiers.fr
[*]hjsung@kaist.ac.kr

ABSTRACT

A three-dimensional (3D) particle image velocimetry (PIV) measurement technique capable of simultaneously monitoring 3D fluid flows and the structure of an arbitrarily moving surface embedded in the flow was proposed with a heavy emphasis on image processing methods [1]. The costs associated with the experimental apparatus were reduced by recording the surface and the trace particles at one image plane without the use of additional cameras or illumination devices. An optimal exposure time for surface and particle imaging was identified using red fluorescent tracer particles in conjunction with a long-pass glass filter. The particle image and surface image were then separated using an image separation process that relied on the feature scaling differences between the particles and the surface texture. A feature detection process and a matching process facilitated estimation of the 3D surface points, and the 3D surface structure was modeled by Delaunay triangulation. The particle volume reconstruction algorithm constrained the voxels inside the surface structure to zero values to minimize ghost particle generation. Volume self-calibration [2] was employed to improve the reconstruction quality and the triangulation accuracy. To conserve computing resources in the presence of numerous zero voxels, the MLOS-SMART reconstruction [3] and the direct non-zero voxel cross-correlation method [3] were applied. Three-dimensional experiments that modeled the flows around an eccentric rotating cylinder and a flapping flag were conducted to validate the present technique.

1. INTRODUCTION

The simultaneous measurements of fluid flows and an arbitrarily moving body have attracted a fair amount of interest for the purposes of understanding fluid-structure interaction problems, such as fish swimming, bird or insect flight, flag flapping, or hydraulic machinery. To economize on the construction of an experimental apparatus and to improve the use of cameras in conventional PIV systems, the moving surfaces and trace particles should be recorded simultaneously at a single image plane in such a way that further image processing may be used to extract additional information. In the case of 2D particle images, a position of surface is instinctively recognizable in the image. By integrating several image processing methods, [4] propose a 2D method which is able to obtain the surface shape and the corresponding displacement. However in contrast to 2D images, the particles in the 3D PIV image generally overlapped with the surface interface facing the fluid and were recorded at the same pixels. Therefore reconstruction of both the 3D surface shape as well as the particle volume associated with 3D surface structure is daunting, thus we propose a PIV measurement technique with an emphasis on image processing methods that simultaneously yields the fluid motion and the shape of the moving surface using a conventional tomographic PIV system.

As the related researches, the motions of a vertical cylinder floating on a wavy water surface and the surrounding fluid motion were measured by [5]. Here, four target dots exposed to the exterior of the water were tracked by two additional cameras, and the 3D motion of the rigid body was estimated in a straightforward manner. The corresponding fluid field was measured using a 3D particle tracking velocimetry implemented with two other cameras. A similar method was applied to a flexible structure by [6] to measure the 3D deformation of a thin elastic plate using a motion tracking system. Recently the present method [1] and the visual hull method [7] have been reported. These methods consider both flow motion and a moving body at the stage of the particle volume reconstruction. The differences between [1] and [7] are the treatment of the moving object and corresponding scale of the targeting object. The present method [1] focuses on both the near-surface flow and the motion of surface, thus the surface occupies almost image region. In contrast to the present method, the visual hull method [7] is able to cover almost region around the moving object instead of abandoning the fluid motion inside the visual hull including the near-surface flow.

2. EXPERIMENTS

Application of the present technique requires careful consideration for the processes by which the particles and surface texture may be imaged simultaneously. In general, a recorded image of a surface is much brighter than an image of scattering from tracer particles due to reflections from the surface. The noise level of the surface frequently overwhelms the particle signal level, and the optimal exposure times can differ enormously. Recording both particles and the surface using a single camera is, therefore, difficult. To address this problem, the imaging contrast between the surface and the particles must be experimentally reduced. One approach is to selectively reduce the surface reflections. The experimental technique used in the present study took advantage of an energy difference between the light reflected by the particles or by the surface. The amplitude of each detected spectral window could then be independently adjusted. Instead of using hollow glass particles, as widely used in aqueous experiments, 31 μm fluorescent particles were used as tracer particles to shift the detection wavelength. The particles were selected to absorb green light (542 nm) and emit red light (612 nm); thus, the scattered light from the tracer particles was shifted. The surface brightness was adjusted by installing a long-pass glass filter with a 550 nm cut-off wavelength before the lens system. This filter reduced green light (532 nm) scattering from the Nd:YAG laser to less than 0.5% of the original value. Note that the transmittance of the emitted red light exceeded 99.9%. To improve visualization of the surface shape, the surface of an experimental body was manually textured using black-colored round dots. Figs. 1(a) and 1(b) show tomographic PIV images of the experimental imaging setup, in which the particles and surface were visualized using a single camera simultaneously. The red particles in the magnified images shown in Figs. 1(c) and 1(d) were then extracted using an image separation method [1].
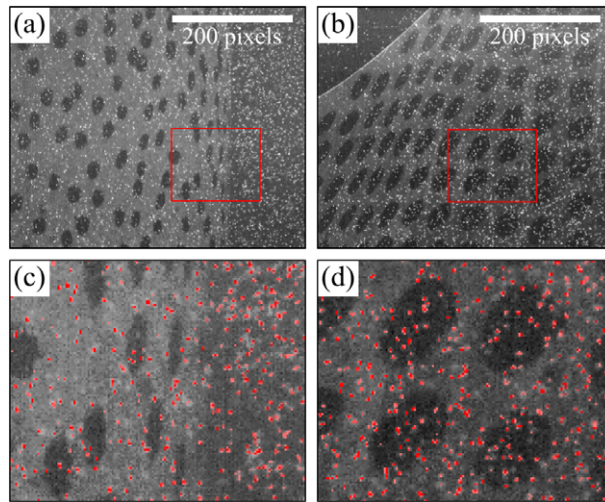

Figure 1   3D PIV images of a moving surface. (a) Flow around an eccentric rotating cylinder. (b) Flow over a flapping flag. (c) and (d) Magnified images of (a) and (b) respectively.

A tomographic PIV measurement system was constructed, as shown in Figs. 2(a) and 2(b). The experiments were performed in an octagonal water tank with a closed test section of dimensions 300 mm (height) × 200 mm (diameter). A volumetric laser sheet was produced using Nd:Yag lasers: a double-pulse system that delivers 200 mJ per 532 nm pulse at 15 Hz. A four-camera system was arranged to record 10-bit images at a resolution of 1280×1024 pixels^2. The laser system and the camera system were synchronized to record PIV image pairs at 15 Hz. Each camera was mounted such that the viewing angle in the horizontal direction was ± 22.5 degrees, perpendicular to the wall of the water tank, and vertically oriented at ± 15.0 degrees. The focal plane of each camera was aligned with a test volume according to the Scheimpflug principle, and 85 mm tilting lens systems set at f/11 were installed. The effective field of view for each camera was 60×50mm^2 at the center plane of the test volume, and the seeding particle density was 0.019 particles per pixel when only particles were present, except at a surface.

The preliminary calibration has been performed by scanning an L-shaped calibration plate with 13 × 19 white dots of 5.0mm spacing on each of the right-angled sides. The voxel positions in space were mapped to each camera with an error of less than 1.5 pixels. This error exceeded the tolerance limits, which is 0.2 pixel accuracy to achieve a fair construction [8]. Therefore the volume self-calibration technique [3] was employed in the present study. The volume self-calibration technique greatly improved the reconstruction qualities of the particles and surface, and further assessment of the tomographic reconstruction method was possible. In addition, an iterative linear least-squares method was applied to the triangulation method in the present study to take advantage of its simple and rapid calculation [9].
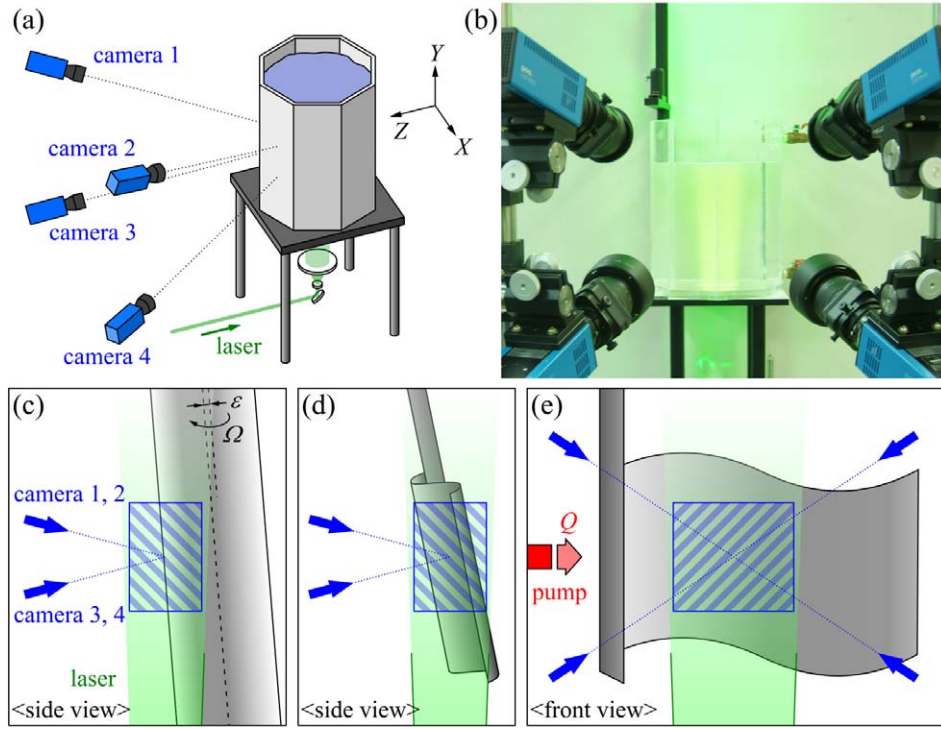
Figure 2 Schematic diagram of the experimental setup and its optical arrangement. (a) Schematic diagram of the tomographic PIV system. (b) Front-view of the experimental apparatus. (c) Flow around an eccentric rotating cylinder. (d) and (e) Flow over a flapping flag.

The method was evaluated using two test flow cases: flow around an eccentric rotating cylinder (Fig. 2(c)) and flow over a flapping flag (Figs. 2(d) and (e)). The flow around a rotating cylinder was measured using a PVC cylinder of diameter $2R = 38$ mm. To guarantee proper illumination over the entire surface, the cylinder was leaned toward the front ($+Z$ direction). The eccentric rotating axis and the surrounding buffering material produced an unpredictable rotating motion as the rotating speed Ω was varied from 30 rpm to 114 rpm. The corresponding average velocities at the surface and the corresponding Reynolds number were $U_0 = 0.0597{\sim}0.227$ m/s and corresponding $Re_R = 1130{\sim}4290$, respectively. The interval between the PIV image pair was set at $4.0{\sim}1.0$ ms. The cylinder surface was polished using 180 grit sandpaper to prevent total reflection from a smooth surface, and was textured using black-colored round dots 1.3 mm in diameter. Flow around the flexible flapping flag was also examined, as shown in Figs. 2(d) and 2(e). To generate a flapping motion, a water pump with an exit diameter $D = 10$ mm generated a jet flow along the horizontal direction ($+X$ direction). The flat flag pole 13 mm in width and 0.5 mm thick obliquely leaned toward the flow direction (${\sim}30$ degrees). Note that the flagpole leaned toward the front, similar to the cylinder. The estimated flow rate was found to be 1.7×10^{-4} m^3/s, and the flow was circulated inside the tank of the closed system. The corresponding maximum velocity of the average velocity field without the flag was measured to be $U_m = 0.487$ m/s. The dimensions of the flag were 110×70 mm^2, and the average diameter of the dots was increased by 2.2 mm to guarantee detection of the surface pattern scale in the image during strong furling. The interframe time, that is, the time between successive PIV image frames, was set to 0.2 ms.

3. IMAGE SEPARATION

During simultaneous recording, a PIV image I (u, v) could be regarded as the summation of a particle image P (u, v) and a surface image S (u, v):

$$I\,(u, v) \approx P\,(u, v) + S\,(u, v) \tag{1}$$

As mentioned earlier, the motivation for separating the images was to facilitate feature analysis when the scale of the particles was much smaller than that of the surface texture. The surface image, which had a relatively large texture, was more robust than the particle image, which was filled with small scattered peaks after application of a Gaussian smoothing function. An estimated threshold image T_E (u, v, σ, c) that could distinguish between the small scattered features, that is, the particles, from the PIV image was introduced as

$$T_E \left(u, \ v, \ \sigma, \ c \right) = \left[\frac{1}{2\pi\sigma^2} \exp\left(-\frac{u^2+v^2}{2\sigma^2} \right) \right] * I\left(u, \ v \right) + c \tag{2}$$

, where σ is the scale of the Gaussian smoothing function, proportional to the particle size, and the constant c should be larger than the maximum noise level of the smoothed surface image. $\sigma = 2.0$ pixels was found to be appropriate for the present experiments. A pixel with intensity above the threshold T_E was assumed to correspond to a particle image. Accordingly, the estimated particle images $P_E(u, v)$ could be expressed as

$$P_E(u, v) = \max\left[\ I(u, v) - T_E(u, v, \sigma, c), \ 0 \ \right]. \tag{3}$$

Since the smoothed particle images contributed to the threshold T_E, T_E was still erroneous. The threshold image needed to be refined once again, according to the following equation, using Eqs. (2) and (3),

$$T\left(u, \ v, \ \sigma, \ c \right) = \left[\frac{1}{2\pi\sigma^2} \exp\left(-\frac{u^2+v^2}{2\sigma^2} \right) \right] * \left[I\left(u, \ v \right) - P_E\left(u, \ v \right) \right] + c. \tag{4}$$

The particle image $P(u, v)$ and the remaining surface image $S_R(u, v)$ could be separated according to the following equation (Figs. 3(b) and 3(c)),

$$P(u, v) = \max\left[\ I(u, v) - T(u, v), \ 0 \ \right],$$
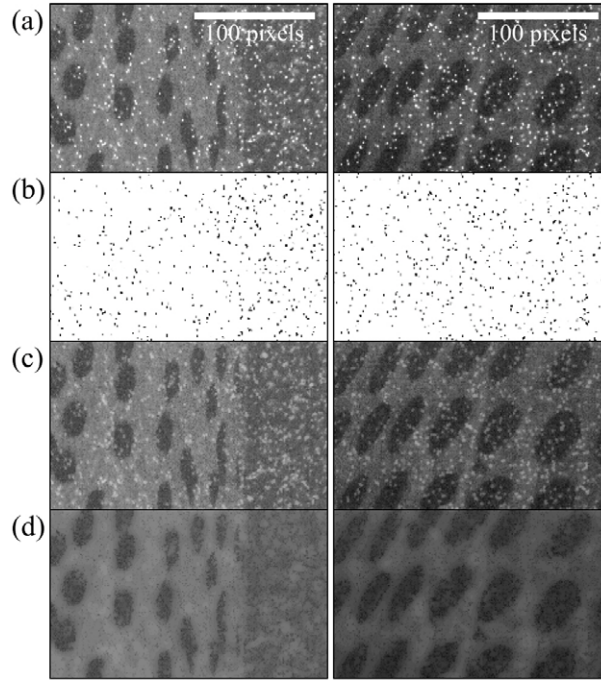$$S_R(u, v) = I(u, v) - P(u, v). \tag{5}$$

Figure 3   Procedure used for image separation; cylinder (*left*) and flag (*right*). (a) Original PIV images $I(u, v)$. (b) Extracted particle images $P(u, v)$, (c) Remaining surface image $S_R(u, v) = S(u, v) + O(u, v)$. (d) Surface image $S(u, v)$.

Individual particles extracted according to Fig. 3(b) covered only 2~3 pixels square, which was sufficient for further tomographic reconstruction. As shown in Fig. 3c, the remaining surface image showed plenty of smudges due to the residues of the extracted particles. To refine this image once again, Eqs. (1) ~ (5) were applied once again with $\sigma' = 4.0$ pixels and $c' = 0.25\ c$. The surface image improved even further, as shown in Fig. 3(d). The resulting mathematical formulation of the final surface image $S(u, v)$ was

$$O(u, v) = \max\left[\ S_R(u, v) - T'(u, v), \ 0 \ \right],$$
$$S(u, v) = S_R(u, v) - O(u, v). \tag{6}$$

where O (u, v) indicates an erroneous term. Hence, Eq. (1) can be rewritten as

$$I (u, v) = P (u, v) + S (u, v) + O (u, v). \tag{7}$$

The surface image S (u, v) was then delivered to the surface reconstruction process prior to the tomographic particle volume reconstruction. The image separation proposed in the present study was an expansion of the particle image treatment proposed by [8], including the background intensity removal, the particle intensity equalization, and the Gaussian smoothing. In comparison with previous studies, the present study utilized the background intensity to obtain the surface image. A corresponding intensity ratio, which is a particle SNR, between the surface image and the intensity value of particle peaks, was obtained about 2.2.

4. SURFACE RECONSTRUCTION

In the experiment, a moving body usually located in the test volume. During the process of particle volume reconstruction, the occupied voxels could be treated as a zero voxel to avoid the generation of ghost particles. The 3D surface structure was essential for determining whether the voxel belonged to the fluid or the moving body. In the present study, round black dots were used as the surface pattern. If the common surface patterns in each image were determined, the 3D position of the surface pattern could be evaluated according to the triangulation method with the known 2D coordinates from the camera images. To perform this operation, a surface pattern must be obtained by image processing techniques, such as feature detection, and then central coordinates of each round dot could be regarded as representative of the surface pattern.

Fig. 4(c) shows a raw partial surface image after the image separation process. Significant noise was present due to the sensitivity of the imaging sensor or the insufficient reflection intensity. To improve the image quality by correcting the noisy pixels, a median filter with a 5 by 5 octagonal kernel including the central pixel, as shown in Fig. 4(a), was employed [10]. In applying the median filter, the intensity of the pixel was replaced by the median intensity of the kernel. Consequently, noise was eliminated, as shown in Figs. 4(b) and 4(d) and the image quality was dramatically improved.
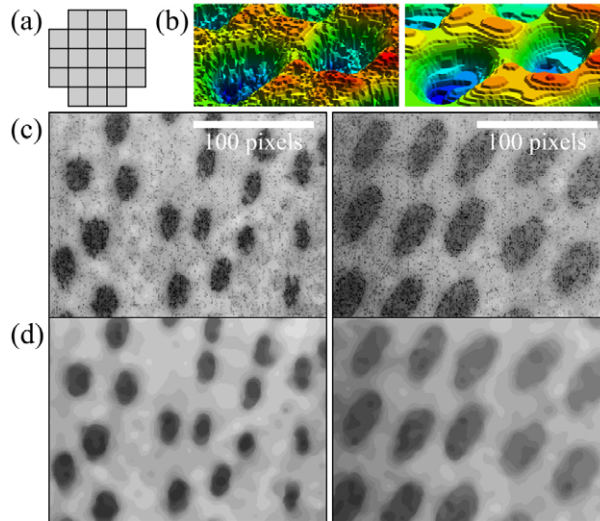

Figure 4   Noise reduction upon application of a median filter. (a) A 5x5 octagonal kernel. (b) Three-dimensional view of the image enhancement after noise reduction for the flag case; before filtering (*left*) and after filtering (*right*). (c) Surface image S (u, v) prior to the noise reduction; cylinder (*left*) and flag (*right*). (d) Surface image S (u, v) after the noise reduction; cylinder (*left*) and flag (*right*).

The next step involved a feature detection process that extracted the surface texture. Because the averaged intensity varied by region due to unequal reflections from the surface, single threshold intensity for deciding whether a pixel is part of a feature was not appropriate. Each feature needed to be considered individually in the context of a region-relevant threshold. A feature detection algorithm for detecting the round dots was proposed in the present study based on the assumption that the round dots formed a closed loop, similar to a contour line, at a certain intensity level. This algorithm essentially sought to fill puddles without exceeding a given size, $2L$ pixels, as illustrated in Fig. 5(a). For a given search pixel $\mathbf{u}_0 = (u_0, v_0)$, a square boundary covering a square region from $(u_0 - L, v_0 - L)$ to $(u_0 + L, v_0 + L)$ was

set. As the threshold t increased, the algorithm determined whether the contour line of intensity equal to S $(u_0, v_0) + t$ extended outside the boundary. In the event of an overflow (the red line in Fig. 5(a)), the most recent t that formed a successful closed loop inside the boundary (blue line in Fig. 5(a)) was set as an appropriate threshold at the searching pixel (u_0, v_0). The inner area of the loop was then selected as a feature image $S_P (u_0, v_0)$. To save on processing time, the search pixels $\mathbf{u}_0$ were selected in $L/5$ intervals in both the u- and v-directions. In the present study, $L = 20$ and 40 pixels were selected respectively for the rotating cylinder and the flapping flag due to the maximum sizes of the dot in the recorded image. A puddle image $S_P (u_0, v_0)$ was obtained from the puddle detection process. From this image, the central coordinate of each puddle was calculated and could be regarded as the geometric center of each feature, as shown in Fig. 5(b).
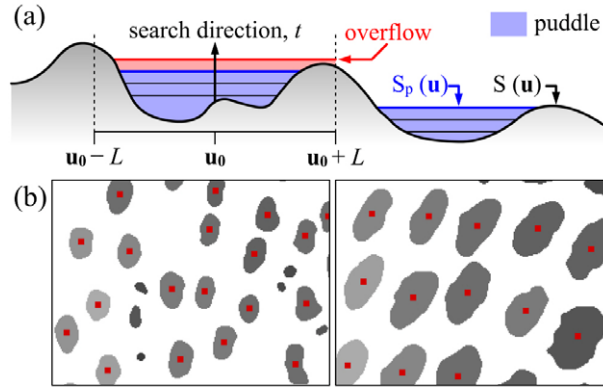

Figure 5   Procedure used for feature detection. (a) Schematic diagram of the puddle detection process. (b) Puddle image $S_P (u_0, v_0)$ and the calculated central coordinates of each puddle; cylinder (*left*) and flag (*right*).

The 3D surface points were reconstructed by applying triangulation to the feature points detected in each camera image. A valid surface point in 3D space should have a minimum residual when projected onto the camera planes and should form a continuous surface face with the other surface points without sudden changes in the shape. To match the features with those in the other cameras, a process of gathering possible pairs was implemented. This operation was identical to the method described for the volume self-calibration [3].
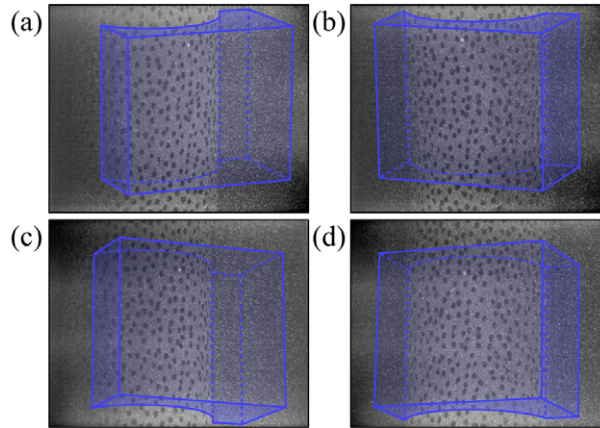

5. TOMOGRAPHIC PIV

Figure 6   Projections of the reconstruction volume onto each camera with overlapping PIV images, for the rotating cylinder experiment: a, b, c, d correspond to cameras 1, 2, 3 and 4, respectively.

A surface structure can occupy a reconstructed particle volume, as shown in Fig. 6. The surface structures must be considered prior to tomographic particle volume reconstruction because the reconstructed voxels with positive values behind the surface will obviously be ghost particles. Therefore the surface height in the Z-direction $Z_S (X, Y)$ must be known for further reconstruction. The first step was to generate surface elements using the reconstructed surface points. The surface elements were defined by three surface points to form triangular elements in 3D space. They could be obtained by applying the 2D Delaunay triangulation to the X-Y plane. As shown in Fig. 7(a), the surface points successfully formed the surface elements, and the corresponding $Z_S (X, Y)$ could then be evaluated by linear interpolation. $Z_S (X, Y)$ could be defined once the surface element covered the (X, Y) positions. A position Z_S, its (X, Y)

is outside of the reconstructed surface, could not be defined, but the real surface may have followed the purple dotted line (Fig. 7(d)). This surface region was not reconstructed because some cameras could not observe the surface pattern underlying the surface structure. To supplement this problem, Z_S (X, Y) at the exterior of the measured surface was corrected using the expression

$$Z_S\left(X,\ Y\right) = Z_S\left(X,\ Y\right)_{\text{inside}} - r_S\sqrt{\left(X - X_{\text{inside}}\right)^2 + \left(Y - Y_{\text{inside}}\right)^2} \tag{8}$$

, where $(X, Y)_{\text{inside}}$ is the closest surface element point to (X, Y). Fig. 7(d) shows the results of this implementation. Although several ghost particles were present, they were negligible in comparison with the real particles.
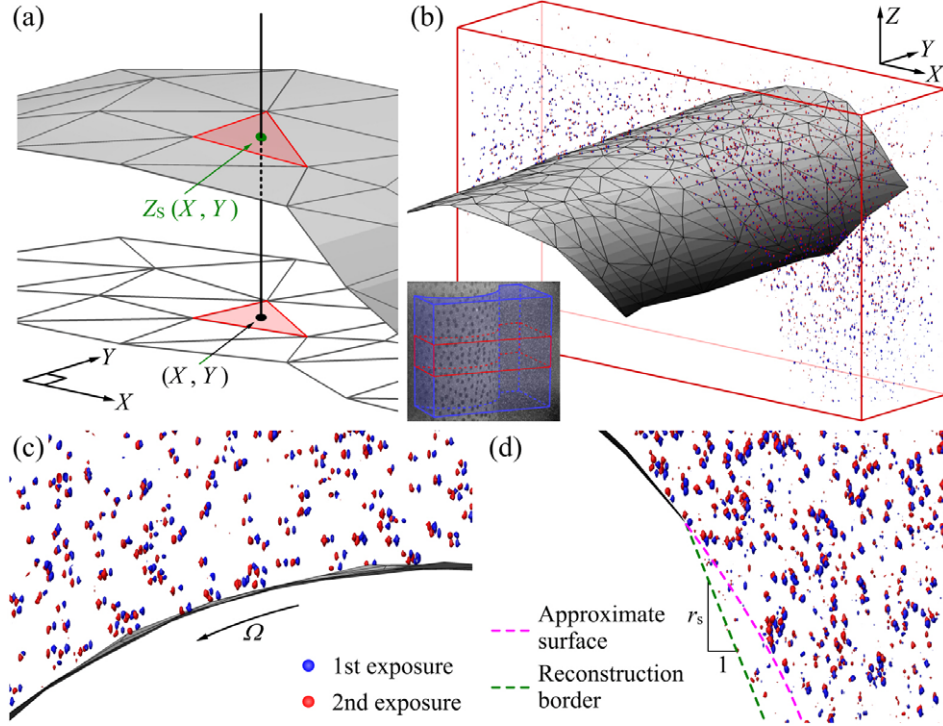

Figure 7   Particle volume reconstruction associated with the surface structure. (a) Triangulated surface structure and surface height Z_S (X, Y). (b) Isosurfaces of a reconstructed particle volume for $Y = -5.5 - +5.5$ mm. (c) Bottom-view near the surface. (d) Schematic diagram of the Z_S (X, Y) estimation exterior to the surface elements.

The particle volume E (X, Y, Z) partially occupied by the surface structure included numerous zero voxels. The sparse distribution of particles also increased the ratio of zero voxels. To reduce the calculation associated with treating the zero voxels, the MLOS-SMART algorithm [4] was adopted. In the present study, the SMART iteration was triggered if Z_j exceeded Z_S through the following SMART iteration,

$$\mathrm{E}\left(X_j,Y_j,Z_j\right)^{k+1} = \begin{cases} \mathrm{E}\left(X_j,Y_j,Z_j\right)^k \prod\limits_{i}^{N_i}\left[\left(\dfrac{\mathrm{P}\left(u_i,v_i\right)}{\sum\limits_{j\in N_i} w_{i,j}\,\mathrm{E}\left(X_j,Y_j,Z_j\right)^k}\right)^{\mu w_{i,j}}\right]^{\frac{1}{N_i}} & ,\text{when } Z_j > Z_S\left(X,\ Y\right) \\[4ex] 0 & ,\text{otherwise} \end{cases} \tag{9}$$

, where N_i is the total number of i-th pixels that contributes to the j-th voxel. A relaxation parameter of $\mu = 4.0$ was chosen, and 40 SMART iterations were applied. In total, $800 \times 720 \times 480$ voxels were reconstructed, and the corresponding dimensions were $44.0 \times 39.6 \times 26.4$ mm^3. Fig. 7(b) shows a partial reconstructed volume for $Y = -5.5 \sim +5.5$ mm (200 voxels) and Figs. 7(c) and 7(d) show a bottom-view near the cylinder surface. The particle pairs could be clearly identified along the rotating direction.

The zero voxels were neglected during calculation of the 3D cross-correlations associated with the particle displacements by calculating the direct non-zero voxel cross-correlation [4]. The maximum displacement was limited to ±4 voxels in the X-, Y-, and Z-directions in this procedure. The displacement vectors were obtained using a 3D extension of the WIDIM algorithm [11] with validation using a 3D local median filter [12]. An interrogation volume of 72^3 voxels (=3.96 mm) with 75% overlap was used, and the corresponding velocity field provided $41 \times 35 \times 23$ vectors with a spatial resolution of $1.98 \times 1.98 \times 1.98$ mm^3 and a depth of field of 21.8 mm.

6. RESULTS AND DISCUSSION

Figs. 8 and 9 show the time-varying Z-heights extracted from the reconstructed cylinder and flag surface structures at $Y = 0$, respectively. These graphs permit estimation of the dynamics of the moving surface. Fig. 8(a) shows the time-varying maximum heights at two rotating speeds. The eccentricity of the rotation resulted in periodic movement. The pulsating frequencies were measured by FFT to be $f = 0.50$ and 1.90, respectively, and the corresponding rotating speeds were $\Omega = 30$ and 114 rpm. Figs. 8(b) and 8(c) show the surface profiles stacked for entire time plotted in Fig. 8(a). Figs. 8(d) and 8(e) show the trajectories for one period. The eccentric radii ε were found to be 0.096R and 0.089R, respectively. The disparity arose from the buffering material inside the cylinder, which acted as a damper.
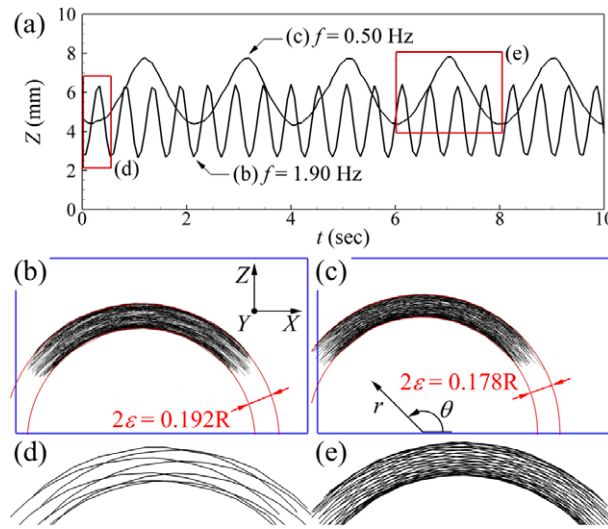

Figure 8   Surface height in the Z-direction at $Y = 0$ for the eccentric rotating cylinder. (a) Time-varying maximum heights. (b) and (d) Surface profile at $\Omega = 30$ rpm. (c) and (e) Surface profile at $\Omega = 114$ rpm.
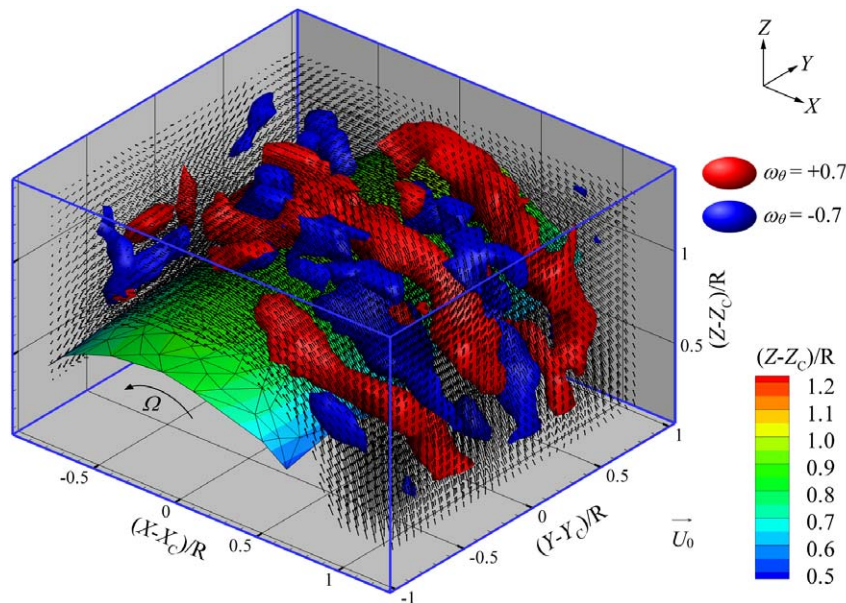

Figure 9   Instantaneous flow field around the reconstructed cylinder.

The instantaneous velocity vectors and reconstructed surface structures of the rapidly rotating cylinder ($\Omega = 114$ rpm and $f = 1.90$ Hz) are shown in Fig. 9. The velocity vectors and length scales were normalized by the average surface velocity $U_0 = R\Omega = 0.227$ m/s and the radius of the cylinder R = 19 mm. The high Reynolds number $Re_R = 4290$ produced an alternating swirling motion that resembled a Taylor–Couette vortex around the cylinder. Fig. 9 shows the vortices along a tangential direction ω_θ. The coordinate system r-θ, which is illustrated in Fig. 8(c), has been defined on the basis of the central axis of the eccentric rotation. This axis was evaluated by using the reconstructed surface. The streamwise vortex structure could not be sustained due to the eccentric rotation.

Fig. 10(a) shows the time-varying maximum and minimum heights for the flapping flag. The motion appeared to be periodic with an average flapping frequency $f = 0.79$ Hz; however, the period of a flapping cycle changed from 1.00 to 1.33 sec as time passed. This period tended to increase as the flapping motion subsided. The flag shapes were stacked, as shown in Fig. 10(b), and a schematic diagram of the pump and flagpole is illustrated along with the test section. On the right side of Fig. 10(b), the stacked surface shape is shown with a diagonal cut along the line of sight from the cameras. The trajectories for one flapping cycle, as indicated in Fig. 10(a), are shown in Figs. 10(c), 10(d), and 10(e). If the flag flapped dramatically, as shown in Fig. 10(c), the surface detection procedure failed because the surface points could not be measured at each camera.
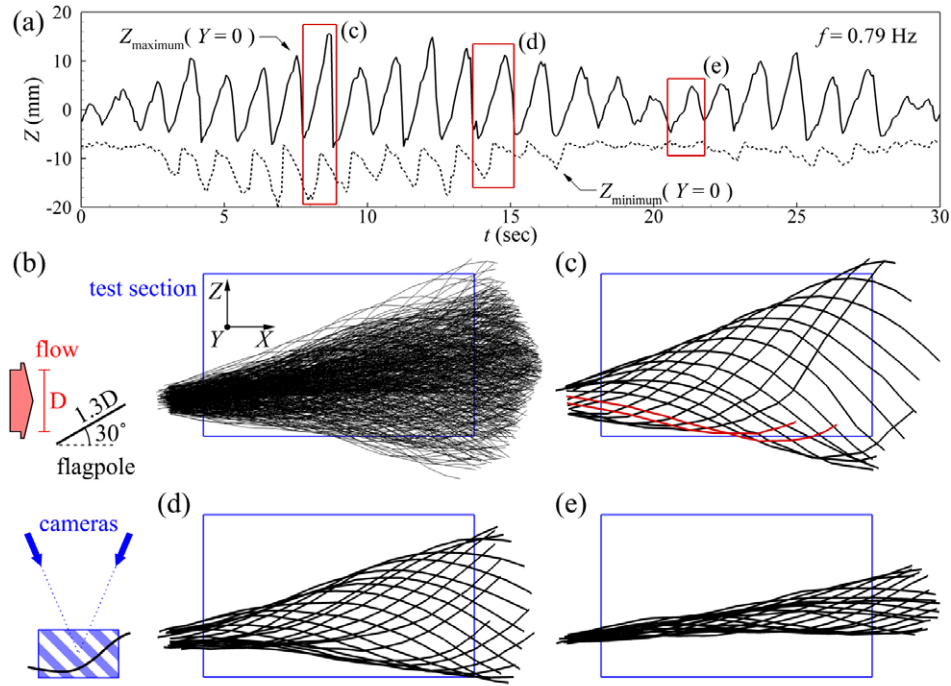

Figure 10 Surface height in the Z-direction at $Y = 0$ for the flapping flag. (a) Maximal and minimal heights. (b) Flag shape at each time step. (c), (d) and (e) show flag shapes during one flapping cycle.

The time-varying velocity fields on the X-Z plane at $Y = 0$ over one flapping cycle are shown in Fig. 11. The maximum velocity field without the flag, $U_m = 0.487$ m/s. The strong stream flow and the surrounding vortex structure are evident as time progressed. A frame rate of 15 Hz yielded a corresponding displacement once $|U|/U_M$ reached unity of about 80% of the horizontal width (X direction); however, the stream diffused and decelerated while flowing over the flag. The surrounding vortices that moved more slowly than the stream also decelerated. The yellow lines indicated probable moving vortices in successive velocity fields. While the flag flapped downward (1~5/20 T and 19~20/20 T) in Fig. 11, the vortices weakened, decelerated, and expanded consistently. In contrast, the movements of the vortices that climbed the flag differed from each other due to the surface shapes and the stream velocity. The vortex that flowed over the convex surface moved faster than the others (9~10/20 T). The concave surface shapes (11~14/20 T and 14~17/20 T), however, slowed the vortices adjacent to the stream.
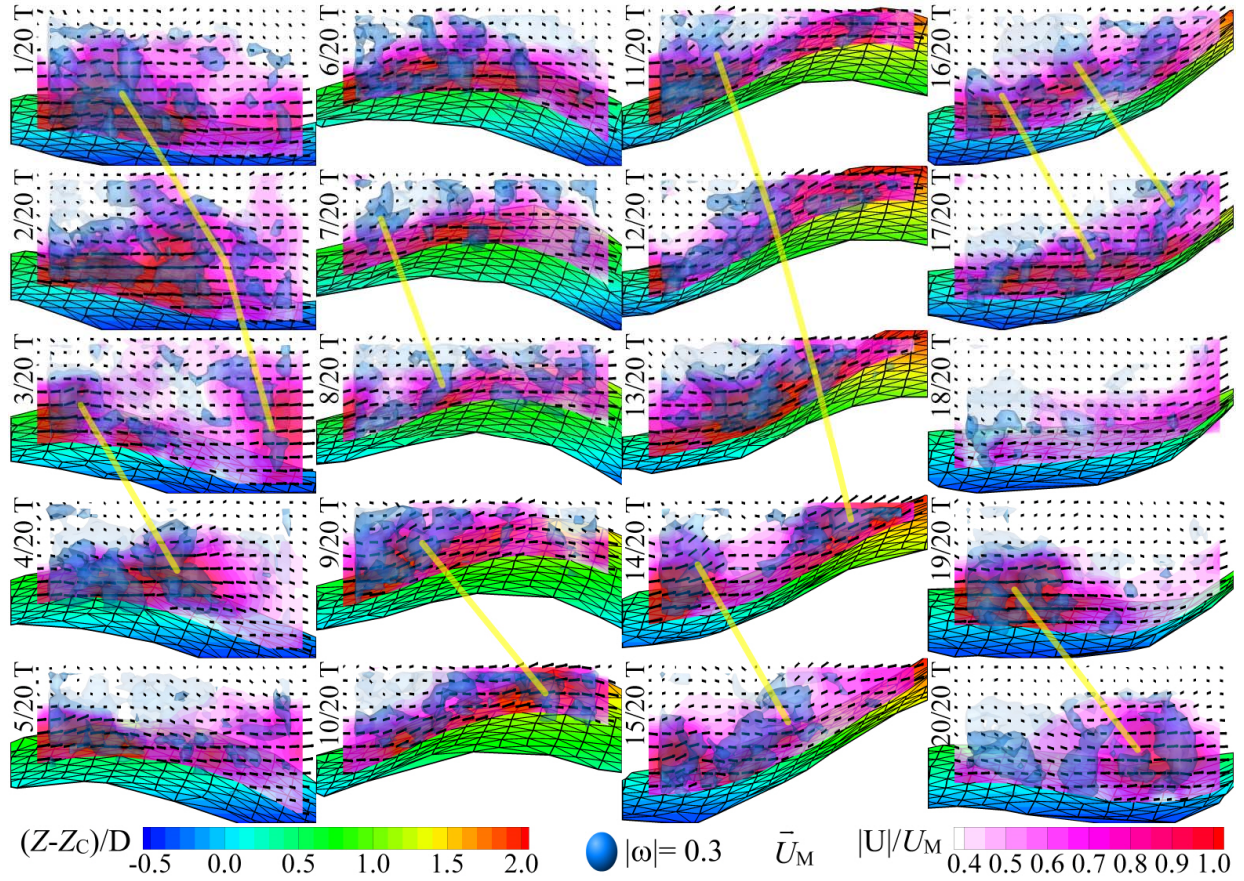
Figure 11 Time varying flow field and the flag motion at $Y = 0$ for one flapping period

7. CONCLUSION

A 3D PIV technique that can model fluid flow in the presence of an arbitrarily moving surface over time was developed in this study. The present technique was used to analyze the surface shape and fluid motions using a conventional tomographic PIV measurement system without the need for additional cameras or illumination devices. The technique also made use of tomographic PIV recording to measure the 3D surface, and it allowed for the simultaneous imaging of the fluid flow and the surface. Red fluorescent particles were used as tracer particles, and a long-pass filter was installed before the lens system to optimize the exposure time for particle and surface imaging by reducing the strong surface reflections. An image separation technique was proposed to obtain pure particle images and a clear surface image by taking advantage of the feature scaling differences between the particles and the surface texture. Round black dots were textured onto the surface and were regarded as surface features. The feature detection process, which consisted of noise reduction and puddle detection, was applied to analyze the surface patterns. The fitness of the mapping that paired particles from different camera views was used to construct a candidate particle correspondence, which enabled modeling of the 3D surface structure using the Delaunay triangulation and morphological evaluation. This method was validated by using pre-described surface shapes. The pure particle image and the reconstructed surface structure were delivered to the tomographic reconstruction process. In this process, the voxel intensities inside the surface structures were constrained to zero values to minimize ghost particle generation. Volume self-calibration was employed to improve the reconstruction quality and triangulation accuracy. Computing resources were conserved by using the MLOS-SMART reconstruction, and the direct non-zero voxel cross-correlation method was applied to efficiently treat the numerous zero voxels. Two experiments were carried out to validate the usefulness of the present method: flow around an eccentric rotating cylinder and flow around a flapping flag. The results of the surface reconstruction agreed well with the actual dynamics of the surface motion. The velocity field and corresponding flow structure as it related to the surface motion were analyzed.

REFERENCES

[1] Jeon YJ, Sung HJ (2012) Three-dimensional PIV measurement of flow around an arbitrarily moving body. Experiments in Fluids 53, 1057-1071

[2] Jeon YJ, Sung HJ (2012) PIV measurement of flow around an arbitrarily moving body. Experiments in fluids 50, 787-798

[3] Wieneke B (2008) Volume self-calibration for 3D particle image velocimetry. Experiments in Fluids 45, 549-556

[4] Atkinson C, Soria J (2009) An efficient simultaneous reconstruction technique for tomographic particle image velocimetry. Experiments in Fluids 47, 553-568

[5] Doh DH, Hwang TG, Jo HJ, Pyeon YB, Cho YB, Tanaka K, Takei M (2006) Non-contact 3D flow-structure interaction measurement (FSIM) system for motion and flow fields. Journal of Visualization 9, 265-274

[6] Hwang TG, Doh DH, Jo HJ, Tsubokura M, Piao B, Kuroda S, Kobayashi T, Tanaka K, Takei M (2007) Analysis of fluid-elastic-structure interactions in an impinging jet with a dynamic 3D-PTV and non-contact 6D-motion tracking system. Chemical Engineering Journal 130, 153–164

[7] Adhikari D, Longmire EK (2012) Visual hull method for tomographic PIV measurement of flow around moving objects. Experiments in Fluids, 943-964

[8] Elsinga GE, Scarano F, Wieneke B, Oudheusden van BW (2006) Tomographic particle image velocimetry. Experiments in Fluids, 933-947

[9] Hartley RI, Sturm P (1997) Triangulation. Computer Vision and Image Understanding 68, 146-157

[10] Russ JC (2002) The image processing handbook. 4th edn. Raleigh, North Carolina

[11] Scarano F, Riethmuller ML (2000) Advances in iterative multigrid PIV image processing. Experiments in Fluids 29, S51-S60

[12] Westerweel J, Scarano F (2005) Universal outlier detection for PIV data" Experiments in Fluids 39 pp.1096–1100

[13] Lee DT, Schachter BJ (1980) Two algorithms for constructing a Delaunay triangulation. International Journal of Computer and Information Sciences 9, 219-242

[14] Lenz RK, Tsai RY (1998) Techniques for calibration of the scale factor and image center for high accuracy 3D machine vision metrology. IEEE Trans. Pattern Analysis and Machine Intelligence 10, 713-720

[15] Novara M, Batenburg KJ, Scarano1 F (2010) Motion tracking-enhanced MART for tomographic PIV. Measurement Science and Technology 21, 035401

[16] Tanaka G, Ishitsu Y, Okamoto K, Madarame H (2002) Simultaneous measurements of free-surface and turbulence interaction using specklegram method and stereo-PIV. In: Proceedings of the 11th international symposium on applications of laser techniques for fluid mechanics, Lisbon, Portugal

[17] Weng J, Chhen, Herniou M (1992) Camera calibration with distortion models and accuracy evaluation. IEEE Transactions on Pattern Analysis and Machine Intelligence 14, 965-980

[18] Worth NA, Nickels TB (2008) Acceleration of Tomo-PIV by estimating the initial volume intensity distribution. Experiments in Fluids 45, 847-856